# Probability Distribution of extreme events in a baroclinic wave laboratory experiment

U. Harlander, I.D. Borcia, C. Rodda, M. Vincze

February 2022

**Abstract**

Atmospheric westerly jet streams are driven by temperature differences between low and high latitudes and the rotation of the Earth. Meandering jet streams and propagating Rossby waves are responsible for the variable weather in mid-latitudes. Moreover, extreme weather events like heat waves and cold spells are part of the jet stream dynamics. Since many years a simple analogue in the form of a simplified laboratory experiment, the differentially heated rotating annulus, has gained insight into the dynamics of the meandering jet stream. In the present study, probability density distributions of extreme events in such long term laboratory experiment are studied and compared to the atmospheric probability density distributions. Empirical distributions of extreme value monthly block data are derived for the experimental and the atmospheric case. Generalized extreme value distributions are fit to the empirical distributions and the distribution parameters are compared. Good agreement can be found, however, the distributions of the experimental data show a shift towards larger extreme values and some explanations for this shift are suggested. The results indicate that the laboratory model might be a useful tool for investigating changes in extreme event distributions due to climate change. In the laboratory context, the change can be modeled by an increase in total temperature accompanied by a reduction of the radial heat contrast.

## 1 Introduction

In the late 40s of the last century *dishpan* experiments have been started to simulate the large-scale atmospheric motions. [7] used a rotating cylindrical vessel with a flat bottom and top. In these experiments the radial temperature difference maintained by using ice cubes for the inner part was hard to control. [9] used an rotating annular vessel consisting of three concentric cylinders (see figure 1) where the narrow-gap outer annulus was filled with warm fluid, the inner cylinder with cold fluid, and the central part was the experimental chamber filled with water or silicon oil. Temperature control was rather easy and hence this kind of experiments were conducted in later years by a large number of

researchers. [5] derived the now famous stability diagram, where the thermal Rossby number was plotted against the Taylor number in double-logarithmic scale. The former measures the thermal wind speed against the rotation speed, the latter plays the role of the Reynolds number for rotating flows. In fact, these two non-dimensional parameters are the similarity parameters that connect the experiment with real atmospheric flows, i.e. the former needs to be small and the latter large for similarity with atmospheric flows. The parameters read

$$Ro_T = \frac{gd\Delta\rho}{\rho_0\Omega^2(b-a)^2}, \qquad Ta = \frac{4\Omega^2(b-a)^5}{\nu^2 d}. \tag{1}$$

$\Delta\rho = \rho_0\alpha\Delta T$, and $g$ the constant of gravity. All the other variables are given in table 1.

Using Hide's annulus experiment, many aspects of atmospheric flows have been studied. Starting point was the confirmation of linear baroclinic instability as a key process of large-scale dynamics [5] but also nonlinear regime transitions and bifurcations to chaotic flows have been analyzed [13]. Of interest was also the nonlinear saturation of baroclinic waves [8], wave-mean flow and wave-wave interactions [6]. Also vascillations and low-frequency variability [11] have been investigated intensively. More recently ideas on optimal growth of baroclinic waves were tested [10]. Moreover, secondary instabilities of the baroclinic jet and the generation of internal gravity waves have been studied [16].

This research showed that the rotating annulus is a good analog to atmospheric dynamics, and this encouraged experiment-oriented geoscientists to study climate-related processes as well. The ideas by [2] on blocking were tested experimentally [22]. Thermally and orographically forced baroclinic waves and the formation of blocking by wave triads have been studied [12]. [21] experimentally investigated the temperature distribution for open and closed baroclinic annulus flows as an analog to Drake passage opening scenarios relevant in paleooceanography. Besides these dynamical aspects of atmospheric and climatic extreme events more statistical features came into the focus as well. For instance, [20] and [17] studied the baroclinic jet variability in so called polar amplification scenarios. However, to our knowledge, no quantitative data analysis on the *distribution* of extreme events have been done so far using the annulus experiment. This is the topic of the present work.

In section 2 we briefly give the experimental setup and in section 3 we present the experimental data retrieved from the annulus experiment forming the basis of our extreme value statistics. In section 4 we present the main result and show the extreme value distributions for the experimental data. We further compare these distributions with the one obtained from reanalysis atmospheric data. The results are discussed in section 4 and in section 5 we give conclusions.

## 2 Experimental setup

The experiment used is a classical Hide-setup with three concentric cylinders (see figure 1). The fluids used for heating and cooling as well as the working

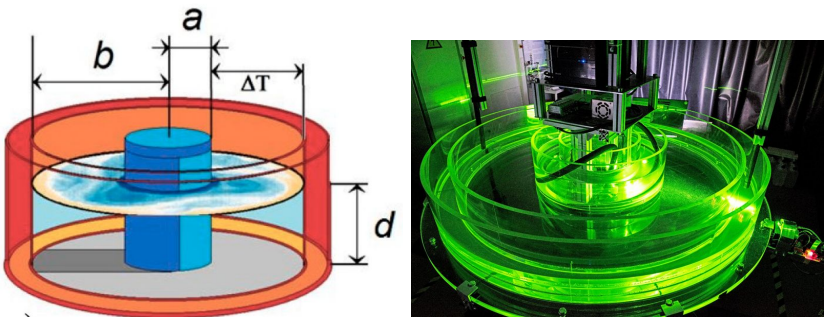


Figure 1: Sketch of experiments (left) and a picture taken in the lab (right).

fluid in the central annular chamber is water. The water in the inner cylinder (outer annulus) is cooled (heated). In contrast to our earlier experiments with applications to climate [20, 21, 17] we used a larger tank with features closer to the atmospheric dynamics [1, 16]. The experimental setup is described in detail in [18] and will not be repeated here. All the relevant experimental parameters can be found in table 1. Note that a rough estimate for the atmosphere gives $Pr = 0.78$, $Ro = 10^{-2}$, and $Ta = 3 \times 10^{31}$. Hence the experiment and the atmosphere fulfill an incomplete similarity only. In fact, applying a sound dimensional analysis would give more than 10 dimensionless parameters [15] and it seems a bit naive to project the atmospheric dynamics to only 3 parameters. However, empirical experience in the laboratory justifies this approach. We can say that, following the diagram by [5], with $1 < Pr < 10$, $Ro << 1$ and $Ta \to \infty$ the experiment and the atmosphere as well are in a geostrophic turbulent regime.

# 3 Data

The surface temperature have been measured by an infra-red (IR) camera (see table 1 for details). The total experimental run lasted for 24 hours with a sampling rate of $\Delta t = 30$s (one IR image per rotation). Taking the angular tank velocity of 2 rpm into account this corresponds to a time period of about 7.9 years of observation. The IR-camera has recorded the surface temperature data only for a segment of the full annulus as shown in figure 2 (left). To give the reader an impression of the surface temperature dynamics we display a hovmoeller plot over a time period of 1 hour from day 380 to day 500 (figure 2 (right). The data have been taken along the azimuthal line segment shown in blue in figure 2 (left). Clockwise traveling baroclinic waves can be identified. However, the wave pattern is rather irregular which is typical for the regime of geostrophic turbulence.

For the extreme value statistics the data have been processed in the following way. First we computed the spatial mean $E_i$ and the spatial variance $V_i$ for

| | | | |
|---|---|---|---|
| **geometry** | | | |
| | inner radius | a (mm) | 350 |
| | outer radius | b (mm) | 700 |
| | gap width | b-a (mm) | 350 |
| | fluid depth | d (mm) | 60 |
| **exp. parameters** | | | |
| | tempeature difference | $\Delta T$ (K) | 4.0 |
| | revolution speed | $\Omega$ (rpm) | 2.0 |
| **fluid properties** | | | |
| | density | $\rho$ $(kgm^{-3})$ | 997 |
| | kin. viscosity | $\nu$ $(m^2s^{-1})$ | 1.004 $\times 10^{-6}$ |
| | therm. conductivity | $\kappa$ $(m^2s^{-1})$ | 0.1434 $\times 10^{-6}$ |
| | exp. coefficient | $\alpha$ (1/K) | 0.207 $\times 10^{-3}$ |
| **similarity parameters** | | | |
| | Prandtl number | Pr=$\nu/\kappa$ | 7.00 |
| | Rossby number | Ro | 0.91 $\times 10^{-2}$ |
| | Taylor number | Ta | 1.52 $\times 10^{10}$ |

Table 1: Parameters of the laboratory experiment. See also figure 1 (left).

| | |
|---|---|
| Image format | 640 × 480 pixel |
| Spectral range | 7.5 $\mu m$ to 14 $\mu m$ |
| Range for measuring/visualization | -40°C to 300°C |
| Thermal sensitivity | < 80mK |
| Measurement accuracy | ±1.5 K |
| Dynamic range | 16 bit |
| Image rate | 60 Hz (NTSC) |

Table 2: Infrared camera technical specifications. The infrared camera used is from Jenoptik, module IR-TCM 640. The software is the IRBIS package developed by InfraTec.

each day $i = 1, 2, ..., 2880$ of the series of IR-images. Second, we evaluated block maximum values:

$$E_{ext}(j) = \max(\{E_i\} \mid \text{i within jth month of the time series}), \tag{2}$$

and

$$V_{ext}(j) = \max(\{V_i\} \mid \text{i within jth month of the time series}). \tag{3}$$

This gives 96 $E_{ext}$ and 96 $V_{ext}$ values of extreme spatial mean temperature and spatial temperature variance. Finally, we consider the deviation from mean values, i.e.

$$E'_{ext}(j) = E_{ext}(j) - < E_{ext}(j) >_j, \quad j = 1, 2, ..., 96, \tag{4}$$

$$V'_{ext}(j) = V_{ext}(j) - < V_{ext}(j) >_j, \quad j = 1, 2, ..., 96, \tag{5}$$

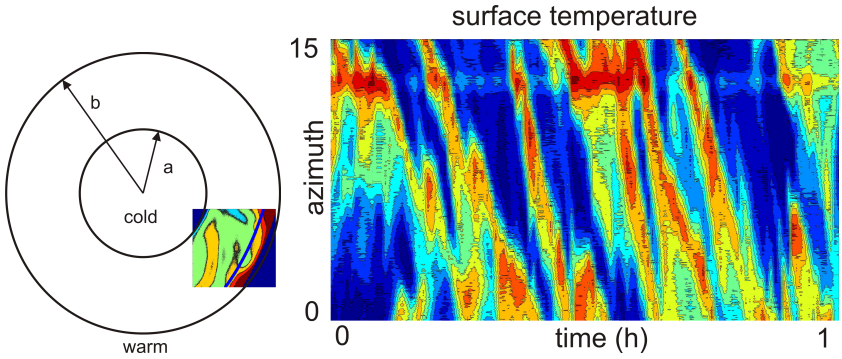


Figure 2: Domain of the working fluid chamber covered by the IR-camera (left). Thick blue line shows the azimuthal sections along which data have been collected to obtain the Hovmoeller plot (right). In this example 1 hour of data are shown. Waves propagate clockwise.

where $< E_{ext}(j) >_j$ and $< V_{ext}(j) >_j$ denote the monthly mean values.

For a later comparison with extreme value distributions in real atmospheric flows we used NCEP reanalysis data (PSL Climate Data Repository/Public/PSL Datasets/PSL Gridded Datasets/ncep.reanalysis) from the 8 year period 2013-2020. We considered daily mean temperature data from the tropopause level of the Atlantic sector (see figure 3). This sector is not much affected by topographic effects that are absent in the experiment. Data from the upper troposphere have shown to be closer to the experimental data since there surface effects are less prominent. Recently it has been shown by [16] that wave energy contributions from the upper atmosphere are qualitatively comparable to upper level experimental data. Using the NCEP data we generated the same block data of $E$ and $V$ as given by (2) and (2).

# 4 Results

## 4.1 Extreme value distributions

The block data of extremes of mean temperature and variance $E'_{ext}(j)$ and $V'_{ext}(j)$ are shown for the experiment in figure 4 and for the NCEP data in figure 5.

Next we defined 20 classes and evaluated empirical probability distributions with the block data. For a better comparison we scaled $E'_{ext}(j)$ by

$$| \, (\max(\{E'_{ext}(j)\} \mid \text{j=1,2,...96} \, )) \, |, \tag{6}$$

the absolut value of the maximum of all 96 $E'_{ext}(j)$ values. For $E'_{ncep}(j)$, $V'_{ext}(j)$, $V'_{ncep}(j)$ we applied the corresponing scaling. The distributions for the experimental data (NCEP data) are shown in figure 6, left column (right column).

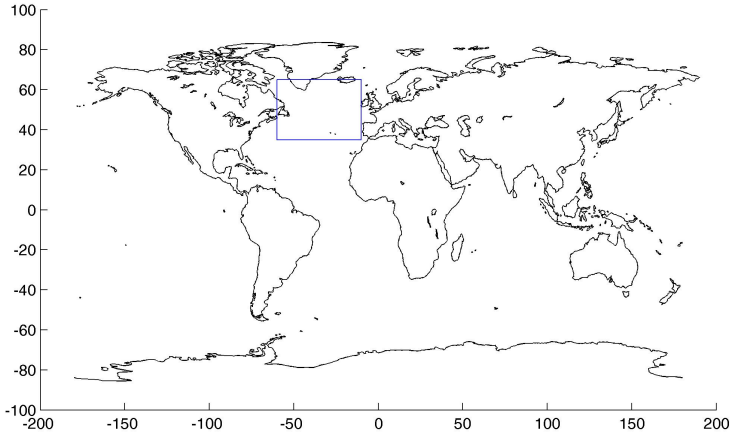


Figure 3: Blue rectangle shows the sector we used for the NCEP data.

By inspection, we find a good qualitative similarity between the experimental and the atmospheric data.

For a more quantitative comparison we fitted the empirical distributions shown in figure 6 to the Generalized Extreme Value (GEV) distribution. The GEV distribution is the standard choice for block data extremes whereas the Generalized Pareto (GP) distribution is more common for Peaks Over Threshold (POT) data, not considered here.

The GEV distribution reads

$$F_{GEV}(x) = \begin{cases} \exp\left(-\left(1+\xi(x-\mu)/\sigma\right)^{-1/\xi}\right) & \text{for} \quad \xi \neq 0, \\ \exp\left(-\exp\left(-(x-\mu)/\sigma\right)\right) & \text{for} \quad \xi = 0, \end{cases} \tag{7}$$

where $\xi$ is the shape parameter, $\sigma$ is the scale parameter, and $\mu$ is the location parameter.

In table 3 we display $\xi$, $\sigma$, and $\mu$ for the experimental (upper two rows, $\mathrm{GEV}^{E,V}_{exp}$) and the atmospheric (lower two rows, $\mathrm{GEV}^{E,V}_{ncep}$) extreme value distributions. They have been estimated by using the MATLAB function `gevfit` using maximum likelihood estimation (for details see e.g. [3] or [14]). We further show the confidence intervals of these parameters ($\xi^{\pm}_{95\%}$, $\sigma^{\pm}_{95\%}$, $\mu^{\pm}_{95\%}$) on the 95% confidence level.

## 4.2 Discussion

From table 3 we see a good agreement between the experimental and atmospheric parameters. This holds in particular for the first moment (extremes of spatial means), i.e. when comparing $\mathrm{GEV}^{E}_{exp}$ and $\mathrm{GEV}^{E}_{ncep}$. The largest deviation can be found for $\mu$. For all parameters there is an uncertainty, largest for

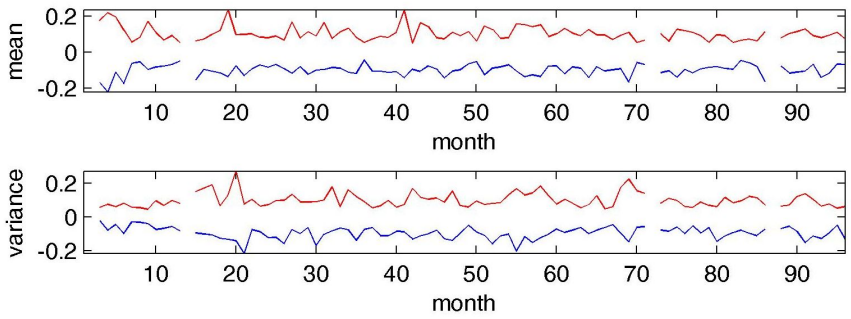


Figure 4: The experimental block data of extremes of mean temperature and variance $E'_{ext}(j)$ (top) and $V'_{ext}(j)$ bottom).

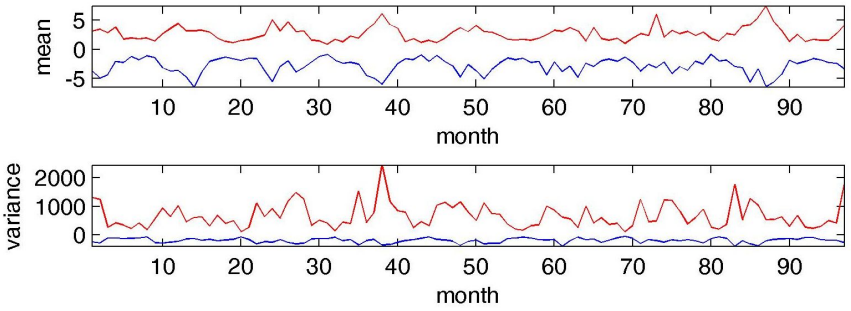


Figure 5: The NCEP block data of extremes of mean temperature and variance $E'_{ext}(j)$ (top) and $V'_{ext}(j)$ bottom).

$\xi$. Such uncertainties come from the fact that the series of monthly extreme values from an 8 year long series are rather short and longer experimental runs should be performed in the future.

Fort the second moment (extremes of spatial variances) the agreement is a bit weaker but still surprisingly good. Here, the largest deviation can be found for $\xi$. Also the uncertainties do not grow compared to the first moment and are again largest for $\xi$.

To make comparison between the extreme value distributions of experimental and atmospheric NCEP data more transparent, we plotted in figure 7 the distributions for all possible parameter combinations of the parameters given in table 3. In blue the experimental distributions are displayed, in red the atmospheric distributions. In the left figure we see the distributions of $E'$ and in the right one the distributions of $V'$. Obviously, there is a systematic shift between the distributions: with respect to the atmospheric distributions, the experimental distributions are shifted towards larger $E'$ and $V'$ values, respectively. However, note that there is also a certain overlap between the distributions.

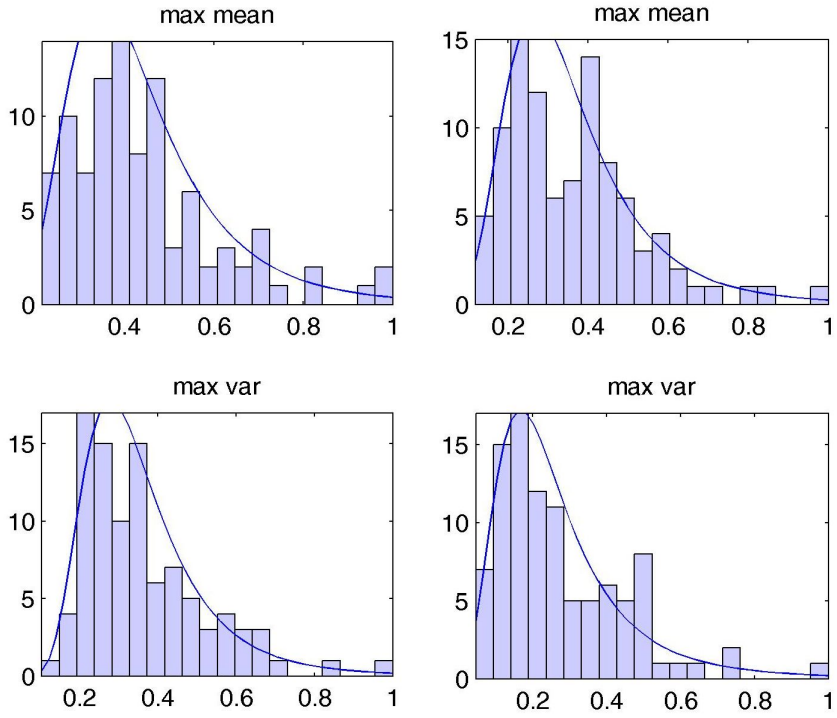


Figure 6: Empirical probability density distributions of $E'_{ext}(j)$ and $V'_{ext}(j)$ values. Left column, experiment; right column, NCEP data.

Why is the probability for values between 0.2 and 0.4 larger for the experimental data than for the atmospheric data? Of course it cannot be expected that the distributions are equal since there are many processes in the atmosphere influencing extreme conditions not included in the simple laboratory experiment. Significant differences are the missing beta-effect and the large Prandtl number in the experiment. Due to the beta-effect the flow is more dispersive which might weaken the chance for extremes. The large $Pr$ leads to more complex flow patterns [4] that might enhance the number of extremes. One other significant differences between the experiment and the atmospheric case is the missing land sea contrast in the experiment. This contrast leads to the development of stationary waves in the atmosphere that can interact with the propagating Rossby wave meanders to form blocking events. The blocking phenomenon effects the frequency of heat waves and cold spells. This effect is not included in the experimental flow. Nevertheless, the rather good match of extreme distribution is a promising fact for laboratory studies on the impact of climate change on the frequency of extreme events. In the lab, climate change can easily be simulated by increasing the temperature and at the same time reducing $\Delta T$ to mimick the effect of arctic amplification that reduces the north-south temperature gradient

| | $\xi$ | $\sigma$ | $\mu$ | $\xi^{\pm}_{95\%}$ | $\sigma^{\pm}_{95\%}$ | $\mu^{\pm}_{95\%}$ |
|---|---|---|---|---|---|---|
| $\mathrm{GEV}^{E}_{exp}$ | 0.1230 | 0.1157 | 0.3621 | -0.0585<br>0.3044 | 0.0967<br>0.1384 | 0.3353<br>0.3889 |
| $\mathrm{GEV}^{V}_{exp}$ | 0.1136 | 0.1055 | 0.2903 | -0.0387<br>0.2660 | 0.0890<br>0.1252 | 0.2666<br>0.3140 |
| $\mathrm{GEV}^{E}_{ncep}$ | 0.1204 | 0.1161 | 0.2809 | -0.0800<br>0.3207 | 0.0965<br>0.1396 | 0.2536<br>0.3082 |
| $\mathrm{GEV}^{V}_{ncep}$ | 0.1996 | 0.1115 | 0.1870 | -0.0020<br>0.4012 | 0.0922<br>0.1347 | 0.1608<br>0.2131 |

Table 3: Estimated parameters for the GEV distribution and the confidence intervals on the 95% level.

on the northern hemisphere [20], [17].

Finally we note that for higher moments like skewness and kurtosis the distributions of experiment and atmosphere differ more. It is likely that for the higher moments the time series are too short to obtain robust extreme value distributions.

# 5 Conclusion

In the present paper we studied daily surface temperature data (one data set per revolution) from a 24 hour thermally driven rotating annulus experiment to derive probability density distributions of extreme values. We considered maximum spatial means and variances within 96 blocks of length 1 month (30 revolutions of the tank). Following extreme value theory the data could be fit to the Generalized Extreme Value (GEV) distribution. This distribution has 3 parameters: the shape parameter $\xi$, the scale parameter $\sigma$, and the location parameter $\mu$. We compared the parameters to the ones from an 8 year series of daily atmospheric data which we have subjected to the exact same statistical procedure. We found the parameters comparable demonstrating that the differentially heated rotating annulus is a promising tool for investigating extreme events in the atmosphere.

As the meandering flow in the experiment, atmospheric jet streams are driven by north-south temperature differences and rotation. Climate change is weakening the north–south temperature gradient, a feature coined Arctic amplification. It might well be that a weakened jet stream shows more meanders which may increase the probability for extreme events like blocking. However, considering the upper levels of troposphere and lower levels of the stratosphere the north-south temperature gradient might even increase which then might imply less frequent extreme events [19]. These are open questions that are usually tackled by numerical modeling. However, in view of our results and the fact that the radial temperature gradient can experimentally be controlled, the rotating annulus laboratory experiment might also be a useful additional tool studying

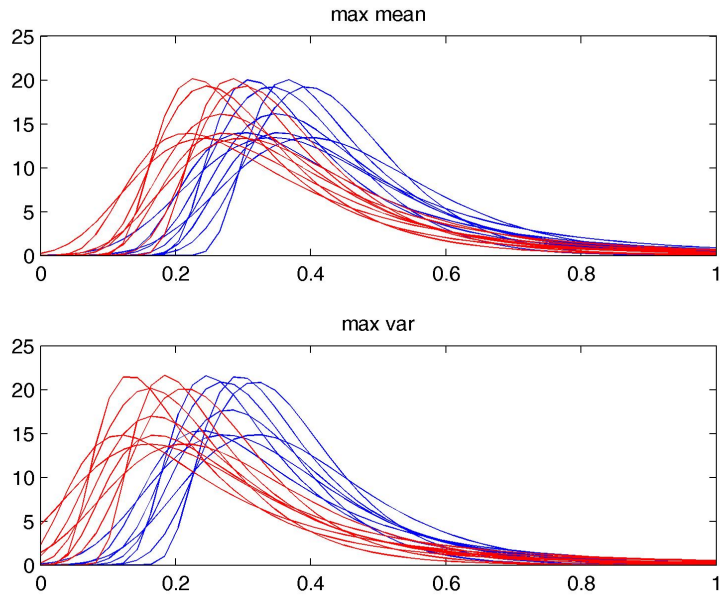


Figure 7: Distributions for parameters $\xi$, $\sigma$, and $\mu$ and all combinations of parameters $\xi^{\pm}_{95\%}$, $\sigma^{\pm}_{95\%}$, and $\mu^{\pm}_{95\%}$ as given in table 3. Blue (red) curves show the experimental (NCEP) data.

the impact of large-scale climate change on the occurrence of extreme events.

**Acknowledgements**
We thank R. Stöbel and S. Rohark for technical support. This work was supported by the *Spontaneous Imbalance Project* (HA 2932/8-1 and HA 2932/8-2) that is part of the research group *Multiscale Dynamics of Gravity Waves* funded by DFG (FOR1898). The work of M.V. was supported by the National Research, Development and Innovation Office (NKFIH) of Hungary under grant FK125024.

# References

[1] S. Borchert, U. Achatz, and M. D. Fruman. "Gravity wave emission in an atmosphere-like configuration of the differentially heated rotating annulus experiment". In: *J. Fluid Mech.* 758 (2014), pp. 287–311.

[2] J. G. Charney and J. G. DeVore. "Multiple-flow equilibria in the atmosphere and blocking". In: *J. Atmos. Sci.* 36 (1979), pp. 1205–1216.

[3] P. Embrechts, C. Klüppelberg, and T. Mikosch. *Modelling Extremal Events for Insurance and Finance*. Springer, New Yorck, 1997.

[4] J. S. Fein and R. L. Pfeffer. "An experimental study of the effects of Prandtl number on thermal convection in a rotating, differentially heated cylindrical annulus of fluid". In: *J. Fluid Mech.* 75 (1976), pp. 81–112.

[5] W. W. Folis and R. Hide. "Thermal convection in a rotating annulus of liquid: effect of viscosity on the transition between axisymmetric and non-axisymmetric flow regimes". In: *J. Atmos. Sci.* 22 (1965), pp. 541–558.

[6] W. G. Früh and P. L. Read. "Wave interactions and the transition to chaos of baroclinic waves in a thermally driven rotating annulus". In: *Phil. Trans. Roy. Soc. London* A355 (1997), pp. 101–153.

[7] D. Fultz et al. "Two-dimensional flow around a circular barrier in a rotating shell". In: *AMS Meteorological Monographs* v. 4 (1959), no. 21.

[8] J. E. Hart. "Wavenumber Selection in Nonlinear Baroclinic Instability". In: *J. Atmos. Sci.* 38.2 (1981), pp. 400–408. DOI: 10.1175/1520-0469(1981)038<0400:WSINBI>2.0.CO;2. URL: https://journals.ametsoc.org/view/journals/atsc/38/2/1520-0469_1981_038_0400_wsinbi_2_0_co_2.xml.

[9] R. Hide. "Some experiments on thermal convection in a rotating liquid". In: *Q. J. R. Meteoro. Soc.* 79 (1953), pp. 294–297.

[10] M. Hoff, U. Harlander, and C. Egbers. "Empirical singular vectors of baroclinic flows deduced from experimental data of a differentially heated rotating annulus". In: *Meteorologische Zeitschrift* 23 (2015), pp. 581–597.

[11] R. S. Lindzen, B. Farrell, and D. Jacqmin. "Vascillations due to wave interference: application to the atmosphere and to annulus experiments". In: *J. Atmos. Sci.* 39 (1981), pp. 14–23.

[12] S. D. Marshall and P. L. Read. "An experimental investigation into topographic resonance in a baroclinic rotating annulus". In: *Geophysical and Astrophysical Fluid Dynamics* 109(4) (2015), pp. 391–421.

[13] O. Morita. "Transition between flow regimes of baroclinic flows in a rotating annulus of fluid, phase transitions". In: *J. Atmos. Sci.* 46 (1990), pp. 213–244.

[14] M. Mudelsee. *Climate time series analysis: classical statistical and bootstrap methods*. Springer, Cham, Switzerland, 2014, 454pp.

[15] P. L. Read. "Dynamics and circulation regimes of terrestrial planets". In: *Planetary and Space Science* 59 (2011), pp. 900–914.

[16] C. Rodda and U. Harlander. "Transition from geostrophic flows to inertia-gravity waves in the spectrum of a differentially heated rotating annulus experiment". In: *J. Atmos. Sci.* 77(8) (2020), pp. 2793–2806.

[17] C. Rodda, U. Harlander, and M. Vincze. "Jet stream variability in a polar warming scenario–a laboratory perspective". In: submitted (2022).

[18] C. Rodda et al. “A new atmospheric-like differentially heated rotating annulus configuration to study gravity wave emission from jets and fronts”. In: *Exp. Fluids* 62(2) (2019). DOI: doi.org/10.1007/s00348-019-2825-z.

[19] M. Stendel et al. “Chapter 15 - The jet stream and climate change”. In: *Climate Change (Third Edition)*. Ed. by Trevor M. Letcher. Third Edition. Elsevier, 2021, pp. 327–357. ISBN: 978-0-12-821575-3. DOI: https://doi.org/10.1016/B978-0-12-821575-3.00015-3. URL: https://www.sciencedirect.com/science/article/pii/B9780128215753000153.

[20] M. Vincze, I. D. Borcia, and U. Harlander. “Temperature fluctuations in a changing climate: an ensemble based experimental approach”. In: *Sci Rep* 7 (2017). DOI: DOI:10.1038/s41598-017-00319-0.

[21] M. Vincze et al. “The Drake Passage opening from an experimental fluid dynamics point of view”. In: *Sci Rep* 11 (2021). DOI: doi.org/10.1038/s41598-021-99123-0.

[22] E. R. Weeks et al. “Transitions Between Blocked and Zonal Flows in a Rotating Annulus with Topography”. In: *Science* 278.5343 (1997), pp. 1598–1601. DOI: 10.1126/science.278.5343.1598. eprint: https://www.science.org/doi/pdf/10.1126/science.278.5343.1598. URL: https://www.science.org/doi/abs/10.1126/science.278.5343.1598.